APPLIED GEOPHYSICS, Vol. 16, No. 4 (December 2019), P. 438—454, 16 Figures.
DOI:10.1007/s11770-019-0783-0

# PML and CFS-PML boundary conditions for a mesh-free finite difference solution of the elastic wave equation*

Sun Cheng-Yu♦[1, 2], Li Shi-Zhong[1, 2], and Xu Ning[1, 2]

**Abstract**: Mesh-free finite difference (FD) methods can improve the geometric flexibility of modeling without the need for lattice mapping or complex meshing process. Radial-basis-function-generated FD is among the most commonly used mesh-free FD methods and can accurately simulate seismic wave propagation in the non-rectangular computational domain. In this paper, we propose a perfectly matched layer (PML) boundary condition for a mesh-free FD solution of the elastic wave equation, which can be applied to the boundaries of the non-rectangular velocity model. The performance of the PML is, however, severely reduced for near-grazing incident waves and low-frequency waves. We thus also propose the complex-frequency-shifted PML (CFS-PML) boundary condition for a mesh-free FD solution of the elastic wave equation. For two PML boundary conditions, we derive unsplit time-domain expressions by constructing auxiliary differential equations, both of which require less memory and are easy for programming. Numerical experiments demonstrate that these two PML boundary conditions effectively eliminate artificial boundary reflections in mesh-free FD simulations. When compared with the PML boundary condition, the CFS-PML boundary condition results in better absorption for near-grazing incident waves and evanescent waves.
**Keywords**: mesh-free finite difference, elastic wave equation, non-rectangular computational domain, perfectly matched layer, complex-frequency-shifted perfectly matched layer

## Introduction

Seismic wave modeling is the basis of geophysical exploration. There are numerous modeling methods, such as finite difference (FD) (Alford et al., 1974; Virieux, 1986), pseudo-spectral (Kosloff and Baysal, 1982), and finite element (Seron et al., 1990). Among these, FD methods have particular simplicity and flexibility and are typically implemented in regular grids. Regular grids lack geometric flexibility, however, and cannot exactly fit model interfaces and boundaries. Furthermore, local

Manuscript received by the Editor November 24, 2018; revised manuscript received December 3, 2019.
*This study is supported by the National Science and Technology Major Project (2016ZX05006-002) and the National Natural Science Foundation of China (Nos. 41874153, 41504097).
1. School of Geosciences, China University of Petroleum (East China), Qingdao 266580, China.
2. Laboratory for Marine Mineral Resources, Qingdao National Laboratory for Marine Science and Technology, Qingdao 266071, China.
♦Corresponding author: Sun Cheng-Yu (Email: suncy@upc.edu.cn).

refinement in critical areas is also hard to achieve. To improve geometric flexibility, structured and unstructured grid methods (Hestholm, 1999; Zhang and Liu, 2002; Zhang and Chen, 2006; Kristek et al., 2010) have been proposed; however, the complex meshing processes and coordinate mapping required by these methods result in significant computational costs. Mesh-free FD methods, such as the irregular lattice method (O'Brien and Bean, 2011), radial-basis-function-generated FD (RBF-FD) method (Flyer et al., 2012, 2014; Martin et al., 2013), mesh-free FD method using the multi-variable Taylor series expansion (Takekawa and Mikada, 2016, 2018), and time-space-domain mesh-free FD based on least squares (Li et al., 2017a), have been more recently developed, and used in seismic wave modeling. Compared with structured and unstructured grids, mesh-free nodes can perfectly fit model boundaries and interfaces. Furthermore, their spatial resolution can be preset according to the velocity of the model. Mesh-free discretization can be used simply and rapidly, thus reducing the cost of improving geometric flexibility. RBF-FD is one of the most popular mesh-free FD methods. The FD based on various radial basis functions (RBFs) has been widely used to solve partial differential equations (Shankar et al., 2015; Flyer et al., 2016a). Current studies on RBF-FD focus predominantly on the limit of increasingly flat RBFs (Driscoll and Fornberg, 2002; Fornberg et al., 2013; Lee et al., 2014) and the inclusion of additional polynomials into RBF-FD approaches (Flyer et al., 2016b; Bayona et al., 2017).

In FD modeling, absorbing boundary conditions are employed to eliminate the spurious reflections caused by model truncation. Among numerous absorbing boundary conditions, the perfectly matched layer (PML) boundary condition, first introduced by Bérenger (1994) for electromagnetic wave simulation, has an effective and stable absorption for incident waves of all angles and all frequencies before discretization. As a result, it is widely used in numerical simulations. Chew and Weedon (1994) mathematically demonstrated that the PML is essentially a coordinate transformation in a complex stretching coordinate system, and Chew and Liu (1996) applied the PML in elastic wave modeling. Nonetheless, the PML also has deficiencies. For example, its reflection coefficient is not exactly zero after discretization; thus, under circumstances such as very thin mesh slices, sources located close to the boundary, and receivers with large offsets, seismic waves can be incident on the PML interface at nearing-grazing angles, causing large spurious reflections (Komatitsch and Martin, 2007). Furthermore, the PML cannot effectively absorb low-frequency waves. To enhance its absorption, Kuzuoglu and Mittra (1996) proposed a more general complex-frequency-shifted (CFS) stretching function in electromagnetic wave modeling. The PML has been approached in both its split-field (Komatitsch and Tromp, 2003) and unsplit-field (Wang and Tang, 2003) forms; however, the split-field approach requires non-physical splitting of wave fields and increases consumption of computer memory. The CFS-PML is also difficult to implement in a split-field form. The unsplit-field approach is based on one of a convolution algorithm (Roden and Gedney, 2000), recursive integration (Drossaert and Giannopoulos, 2007; Zhang et al., 2009; Zhang et al., 2010), or auxiliary differential equations (ADEs) (Zhang and Shen, 2010). Compared with the convolution algorithm, recursive integration or ADEs can make the unsplit PML easier to implement. PML and CFS-PML are often used for first-order wave equations; however, second-order wave equations have simpler forms and are more suitable for numerical simulations. Komatitsch and Tromp (2003) derived the PML expressions for a second-order wave equation by splitting the fields. Third-order temporal derivatives also arise and require the introduction of ADEs. Ma et al. (2014) and Gao et al. (2015) proposed unsplit PML and unsplit CFS-PML expressions for second-order acoustic wave equations. These two unsplit boundary conditions involve neither a convolution algorithm nor high-order temporal derivatives and can thus be easily implemented.

In this paper, we introduce RBF-FD for solving seismic wave equations. We then derive PML and CFS-PML formulations for polygonal model boundaries. Finally, we apply these PML boundary conditions in mesh-free FD simulations of the elastic wave equation. Both PML boundary conditions are applicable to both mesh-free modeling and regular-grid modeling. Numerical results confirm the advantage of RBF-FD, which can simply and efficiently achieve high accuracy and geometric flexibility, demonstrating the effectiveness of the use of two PML boundary conditions and the advantage of the CFS-PML for absorbing near-grazing and evanescent waves.

## Radial-basis-function-generated finite difference method

When using FD methods, the spatial derivative

can be represented by the weighted sum of wave field values at all stencil nodes. For mesh-free FD methods, the nodes are usually irregularly distributed, leading to improved geometric flexibility but also an increase in the difficulty of determining FD coefficients.

RBF-FD is one of the most popular mesh-free FD methods. In the RBF-FD stencil, the approximation of operator $L$ (such as $\partial/\partial x$, $\partial^2/(\partial x\partial z)$, and $\partial^2/\partial x^2$) at the center node $\mathbf{x}_0$ is represented as the weighted sum of wave field values at all $n + 1$ stencil nodes as follows (Martin et al., 2015):

$$Lf(\mathbf{x})\big|_{\mathbf{x}=\mathbf{x}_0} \approx \sum_{i=0}^{n} c_i f(\mathbf{x}_i), \tag{1}$$

where $c_i$ is the mesh-free FD coefficient of node $i$, $\mathbf{x}_i$ is the position of node $i$, and $c_i$ can be determined by solving a linear system as follows (Martin et al., 2015):

$$\begin{bmatrix} \phi(\|\mathbf{x}_0-\mathbf{x}_0\|) & \phi(\|\mathbf{x}_1-\mathbf{x}_0\|) & \cdots & \phi(\|\mathbf{x}_n-\mathbf{x}_0\|) \\ \phi(\|\mathbf{x}_0-\mathbf{x}_1\|) & \phi(\|\mathbf{x}_1-\mathbf{x}_1\|) & \cdots & \phi(\|\mathbf{x}_n-\mathbf{x}_1\|) \\ \vdots & \vdots & \ddots & \vdots \\ \phi(\|\mathbf{x}_0-\mathbf{x}_n\|) & \phi(\|\mathbf{x}_1-\mathbf{x}_n\|) & \cdots & \phi(\|\mathbf{x}_n-\mathbf{x}_n\|) \end{bmatrix} \begin{bmatrix} c_0 \\ c_1 \\ \vdots \\ c_n \end{bmatrix} = \begin{bmatrix} L\phi(\|\mathbf{x}-\mathbf{x}_0\|)\big|_{\mathbf{x}_0} \\ L\phi(\|\mathbf{x}-\mathbf{x}_1\|)\big|_{\mathbf{x}_0} \\ \vdots \\ L\phi(\|\mathbf{x}-\mathbf{x}_n\|)\big|_{\mathbf{x}_0} \end{bmatrix}, \tag{2}$$

or in abbreviated notation, $\mathbf{Ac} = L\phi$.

Here, we use the inverse multiquadric radial function $\phi(r) = 1/\sqrt{1+(\varepsilon r)^2}$ for RBF-FD, where $r$ is the distance between two nodes and $\varepsilon$ is the shape parameter controlling the condition number of coefficient matrix **A**. When the condition numbers of coefficient matrices are in the range of $10^6$–$10^8$, RBF-FD can achieve a good compromise between stability and accuracy. Moreover, a key feature of RBF-FD is the fact that one can impose additional functions (typically polynomials) in equation (2) to improve the convergence rate and overcome the stagnation error (Flyer et al., 2016b). For instance, adding Taylor monomials $(1, x, z)$ to equation (2) obtains the following (Larsson et al., 2013):

$$\begin{bmatrix} & & & 1 & \Delta x_0 & \Delta z_0 \\ & \mathbf{A} & & \vdots & \vdots & \vdots \\ & & & 1 & \Delta x_n & \Delta z_n \\ 1 & \cdots & 1 & & & \\ \Delta x_0 & \cdots & \Delta x_n & & 0 & \\ \Delta z_0 & \cdots & \Delta z_n & & & \end{bmatrix} \begin{bmatrix} & & \\ & \mathbf{c} & \\ & & \\ c_{n+1} & & \\ c_{n+2} & & \\ c_{n+3} & & \end{bmatrix} = \begin{bmatrix} L\phi(\|\mathbf{x}-\mathbf{x}_0\|)\big|_{\mathbf{x}_0} \\ \vdots \\ L\phi(\|\mathbf{x}-\mathbf{x}_n\|)\big|_{\mathbf{x}_0} \\ L1\big|_{\mathbf{x}_0} \\ Lx\big|_{\mathbf{x}_0} \\ Lz\big|_{\mathbf{x}_0} \end{bmatrix}, \tag{3}$$

where $(\Delta x_i, \Delta z_i) = (x_i, z_i) - (x_0, z_0)$. $c_{n+1}$, $c_{n+2}$, and $c_{n+3}$ are auxiliary coefficients and will be discarded after solving equation (3). Note that in order to avoid singularity of the matrix in equation (3), the number of additional rows must not exceed the number of rows in matrix **A**.

## Two boundary conditions for mesh-free FD methods

The traditional FD computational domains are rectangular. Mesh-free FD methods can simulate seismic wave propagation in the non-rectangular computational domain. Boundaries of the objective zone may take the form of slanted straight lines. Here, we use the straightforward expanding strategy (Li et al., 2017b) to generate an absorbing-zone nodal distribution suitable for the polygonal objective zone. The straightforward expanding strategy can be divided into two steps. We first sample the model boundary to determine the sampled boundary nodes and corresponding outward normal directions and then expand absorbing-zone nodes on the basis of sampled nodes and their outward normal directions. In the case of corner nodes where two adjacent boundaries intersect, we consider that the corner node has two outward normal directions $\tilde{\mathbf{n}}_1$ and $\tilde{\mathbf{n}}_2$, and that these nodes are distributed on hypothetical arcs formed by the rotation from $\tilde{\mathbf{n}}_1$ and $\tilde{\mathbf{n}}_2$ with the corner node as the pivot.

In Cartesian coordinate systems, the second-order elastic wave equation can be expressed as

$$\begin{aligned} -\rho\omega^2 U &= (\lambda+2\mu)\frac{\partial^2 U}{\partial x^2} + \mu\frac{\partial^2 U}{\partial z^2} + (\lambda+\mu)\frac{\partial^2 W}{\partial x\partial z}, \\ -\rho\omega^2 W &= \mu\frac{\partial^2 W}{\partial x^2} + (\lambda+2\mu)\frac{\partial^2 W}{\partial z^2} + (\lambda+\mu)\frac{\partial^2 U}{\partial x\partial z}, \end{aligned} \tag{4}$$

where $U$ and $W$ are the horizontal and vertical

displacement components in the frequency domain, respectively; $\lambda$ and $\mu$ are the Lamé coefficients; $\rho$ is density; and $\omega$ denotes angular frequency. To obtain absorbing properties in the PML, a complex coordinate transformation is usually performed on the $x$ and $z$ directions in the absorbing-zone of the Cartesian coordinate system in order to transform the seismic wave equation into a stretched-coordinate domain. For equation (4), we have

$$-\rho\omega^2 U = (\lambda+2\mu)\frac{1}{s_x}\frac{\partial}{\partial x}\left(\frac{1}{s_x}\frac{\partial U}{\partial x}\right)+\mu\frac{1}{s_z}\frac{\partial}{\partial z}\left(\frac{1}{s_z}\frac{\partial U}{\partial z}\right) + (\lambda+\mu)\frac{1}{s_x}\frac{\partial}{\partial x}\left(\frac{1}{s_z}\frac{\partial W}{\partial z}\right), \tag{5a}$$

$$-\rho\omega^2 W = \mu\frac{1}{s_x}\frac{\partial}{\partial x}\left(\frac{1}{s_x}\frac{\partial W}{\partial x}\right)+(\lambda+2\mu)\frac{1}{s_z}\frac{\partial}{\partial z}\left(\frac{1}{s_z}\frac{\partial W}{\partial z}\right) + (\lambda+\mu)\frac{1}{s_x}\frac{\partial}{\partial x}\left(\frac{1}{s_z}\frac{\partial U}{\partial z}\right), \tag{5b}$$

where $s_x$ and $s_z$ are complex stretching functions in the $x$ and $z$ directions, respectively. However, since the truncated boundaries may not be horizontal or vertical, we transform the elastic wave equation into a rotated-coordinate system with an outward normal direction $\tilde{\mathbf{n}}$ from the truncated boundary as a positive axis and transform this elastic wave equation into its corresponding stretched-coordinate domain. The specific process will be described in detail below.

## The slanted boundary

As shown in Figure 1, the absorbing-zone node $R$, which is expanded based on a slanted boundary, has an outward normal direction $\tilde{\mathbf{n}}$. We transform the wave fields at all nodes in the FD stencil centered on node $R$ and then transform elastic wave equation into a rotated-coordinate system with the direction $\tilde{\mathbf{n}}$ as a positive axis such that equation (4) becomes

$$-\rho\omega^2\tilde{U} = (\lambda+2\mu)\frac{\partial^2\tilde{U}}{\partial\tilde{\mathbf{n}}^2}+\mu\frac{\partial^2\tilde{U}}{\partial\hat{\mathbf{n}}^2}+(\lambda+\mu)\frac{\partial^2\tilde{W}}{\partial\tilde{\mathbf{n}}\partial\hat{\mathbf{n}}},$$
$$-\rho\omega^2\tilde{W} = \mu\frac{\partial^2\tilde{W}}{\partial\tilde{\mathbf{n}}^2}+(\lambda+2\mu)\frac{\partial^2\tilde{W}}{\partial\hat{\mathbf{n}}^2}+(\lambda+\mu)\frac{\partial^2\tilde{U}}{\partial\tilde{\mathbf{n}}\partial\hat{\mathbf{n}}}, \tag{6}$$

where $\hat{\mathbf{n}}$ represents both the direction perpendicular to $\tilde{\mathbf{n}}$, and the positive axis of a rotated-coordinate system,

$$\tilde{U} = U\cos\theta + W\sin\theta,$$
$$\tilde{W} = -U\sin\theta + W\cos\theta, \tag{7}$$

in which $\theta$ is the angle between the outward normal direction $\tilde{\mathbf{n}}$ and the horizontal direction, $\theta\in[0,2\pi]$.

In the stretched-coordinate domain corresponding to the rotated-coordinate system, equation (6) becomes

$$-\rho\omega^2\tilde{U} = (\lambda+2\mu)\frac{1}{s_{\tilde{\mathbf{n}}}}\frac{\partial}{\partial\tilde{\mathbf{n}}}\left(\frac{1}{s_{\tilde{\mathbf{n}}}}\frac{\partial\tilde{U}}{\partial\tilde{\mathbf{n}}}\right)+\mu\frac{\partial^2\tilde{U}}{\partial\hat{\mathbf{n}}^2} + (\lambda+\mu)\frac{1}{s_{\tilde{\mathbf{n}}}}\frac{\partial^2\tilde{W}}{\partial\tilde{\mathbf{n}}\partial\hat{\mathbf{n}}}, \tag{8a}$$

$$-\rho\omega^2\tilde{W} = \mu\frac{1}{s_{\tilde{\mathbf{n}}}}\frac{\partial}{\partial\tilde{\mathbf{n}}}\left(\frac{1}{s_{\tilde{\mathbf{n}}}}\frac{\partial\tilde{W}}{\partial\tilde{\mathbf{n}}}\right)+(\lambda+2\mu)\frac{\partial^2\tilde{W}}{\partial\hat{\mathbf{n}}^2} + (\lambda+\mu)\frac{1}{s_{\tilde{\mathbf{n}}}}\frac{\partial^2\tilde{U}}{\partial\tilde{\mathbf{n}}\partial\hat{\mathbf{n}}}, \tag{8b}$$

where $s_{\tilde{\mathbf{n}}}$ is the stretching function. Note that absorbing-zone nodes expanded based on the slanted boundary have the same outward normal direction $\tilde{\mathbf{n}}$, and it is necessary only to consider the absorption of seismic waves along the direction $\tilde{\mathbf{n}}$. Compared with equation (5), equation (8) has more simplified formulations for further derivation. Following this, we can obtain PML and CFS-PML expressions suitable for the slanted boundary.

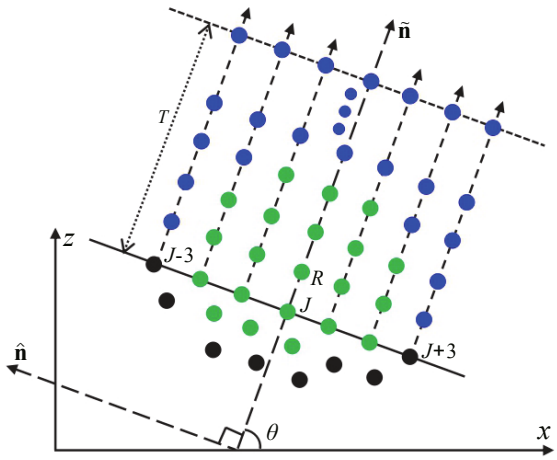


**Fig. 1 Illustration of expanding absorbing-zone nodes for the slanted boundary.** Black dots represent mesh-free discrete nodes in the objective zone, blue dots are absorbing-zone nodes, and green dots are all nodes in the FD stencil centered on node *R*.

### The PML boundary condition for the slanted boundary

The stretching function is defined as (Drossaert and Giannopoulos, 2007)

$$s_{\tilde{\mathbf{n}}} = 1 + \frac{d_{\tilde{\mathbf{n}}}}{\mathrm{i}\omega}, \tag{9}$$

where $d_{\tilde{\mathbf{n}}}$ is the attenuation factor that exponentially attenuates the amplitude of the wave field along direction $\tilde{\mathbf{n}}$. For the attenuation factor (Komatitsch and Martin, 2007; Drossaert and Giannopoulos, 2007), we use

$$d_{\tilde{\mathbf{n}}} = \frac{3v_{\max}\ln\left(1/R_c\right)}{2T}\left(\frac{l}{T}\right)^2, \tag{10}$$

where $v_{\max}$ is the maximum P-wave velocity, $T$ is the thickness of the absorbing-zone, $l$ is the distance between the expanded node and its corresponding sampled boundary node, and $R_c$ is the theoretical reflection coefficient. The relationship between $R_c$ and the PML width $N$ follows a logarithmic equation (Zhang and Shen, 2010) as follows: $\log_{10}(R_c) = -(\log_{10}(N)-1)/\log_{10}(2)-3$.

By constructing ADEs, we can obtain the unsplit PML formulations. For simplicity, we consider equation (8a) as an example. Equation (8a) becomes

$$-\rho\omega^2\tilde{U} = (\lambda+2\mu)\left[-\frac{(\mathrm{i}\omega)^2 d'_{\tilde{\mathbf{n}}}}{(\mathrm{i}\omega+d_{\tilde{\mathbf{n}}})^3}\frac{\partial\tilde{U}}{\partial\tilde{\mathbf{n}}} + \frac{(\mathrm{i}\omega)^2}{(\mathrm{i}\omega+d_{\tilde{\mathbf{n}}})^2}\frac{\partial^2\tilde{U}}{\partial\tilde{\mathbf{n}}^2}\right] + \mu\frac{\partial^2\tilde{U}}{\partial\hat{\mathbf{n}}^2} + (\lambda+\mu)\frac{\mathrm{i}\omega}{\mathrm{i}\omega+d_{\tilde{\mathbf{n}}}}\frac{\partial^2\tilde{W}}{\partial\tilde{\mathbf{n}}\partial\hat{\mathbf{n}}}, \tag{11}$$

where $d'_{\tilde{\mathbf{n}}}$ is the first-order derivative of $d_{\tilde{\mathbf{n}}}$ along direction $\tilde{\mathbf{n}}$. Introducing a variable, $\psi = \mathrm{i}\omega + d_{\tilde{\mathbf{n}}}$ and substituting it into equation (11), we obtain

$$\begin{aligned}-\rho\omega^2\tilde{U} = {}& (\lambda+2\mu)\frac{\partial^2\tilde{U}}{\partial\tilde{\mathbf{n}}^2} + \mu\frac{\partial^2\tilde{U}}{\partial\hat{\mathbf{n}}^2} + (\lambda+\mu)\frac{\partial^2\tilde{W}}{\partial\tilde{\mathbf{n}}\partial\hat{\mathbf{n}}} \\ & -\left[(\lambda+2\mu)\left(\frac{d'_{\tilde{\mathbf{n}}}}{\psi}\frac{\partial\tilde{U}}{\partial\tilde{\mathbf{n}}} + \frac{2d_{\tilde{\mathbf{n}}}}{\psi}\frac{\partial^2\tilde{U}}{\partial\tilde{\mathbf{n}}^2}\right) + (\lambda+\mu)\frac{d_{\tilde{\mathbf{n}}}}{\psi}\frac{\partial^2\tilde{W}}{\partial\tilde{\mathbf{n}}\partial\hat{\mathbf{n}}}\right] \\ & +(\lambda+2\mu)\left(\frac{2d_{\tilde{\mathbf{n}}}d'_{\tilde{\mathbf{n}}}}{\psi^2}\frac{\partial\tilde{U}}{\partial\tilde{\mathbf{n}}} + \frac{d_{\tilde{\mathbf{n}}}^2}{\psi^2}\frac{\partial^2\tilde{U}}{\partial\tilde{\mathbf{n}}^2}\right) - (\lambda+2\mu)\frac{d_{\tilde{\mathbf{n}}}^2 d'_{\tilde{\mathbf{n}}}}{\psi^3}\frac{\partial\tilde{U}}{\partial\tilde{\mathbf{n}}}.\end{aligned} \tag{12}$$

Introducing an auxiliary

$$\begin{aligned}\tilde{U}_1 = {}& \left[(\lambda+2\mu)\left(\frac{d'_{\tilde{\mathbf{n}}}}{\psi}\frac{\partial\tilde{U}}{\partial\tilde{\mathbf{n}}} + \frac{2d_{\tilde{\mathbf{n}}}}{\psi}\frac{\partial^2\tilde{U}}{\partial\tilde{\mathbf{n}}^2}\right) + (\lambda+\mu)\frac{d_{\tilde{\mathbf{n}}}}{\psi}\frac{\partial^2\tilde{W}}{\partial\tilde{\mathbf{n}}\partial\hat{\mathbf{n}}}\right] \\ & -(\lambda+2\mu)\left(\frac{2d_{\tilde{\mathbf{n}}}d'_{\tilde{\mathbf{n}}}}{\psi^2}\frac{\partial\tilde{U}}{\partial\tilde{\mathbf{n}}} + \frac{d_{\tilde{\mathbf{n}}}^2}{\psi^2}\frac{\partial^2\tilde{U}}{\partial\tilde{\mathbf{n}}^2}\right) + (\lambda+2\mu)\frac{d_{\tilde{\mathbf{n}}}^2 d'_{\tilde{\mathbf{n}}}}{\psi^3}\frac{\partial\tilde{U}}{\partial\tilde{\mathbf{n}}},\end{aligned} \tag{13}$$

equation (12) is rewritten as

$$-\rho\omega^2\tilde{U} = (\lambda+2\mu)\frac{\partial^2\tilde{U}}{\partial\tilde{\mathbf{n}}^2} + \mu\frac{\partial^2\tilde{U}}{\partial\hat{\mathbf{n}}^2} + (\lambda+\mu)\frac{\partial^2\tilde{W}}{\partial\tilde{\mathbf{n}}\partial\hat{\mathbf{n}}} - \tilde{U}_1. \tag{14}$$

Multiplying both sides of equation (13) by $\psi$, we obtain

$$\begin{aligned}\psi\tilde{U}_1 = {}& (\lambda+2\mu)\left(d'_{\tilde{\mathbf{n}}}\frac{\partial\tilde{U}}{\partial\tilde{\mathbf{n}}} + 2d_{\tilde{\mathbf{n}}}\frac{\partial^2\tilde{U}}{\partial\tilde{\mathbf{n}}^2} - d_{\tilde{\mathbf{n}}}\tilde{U}_2\right) \\ & +(\lambda+\mu)d_{\tilde{\mathbf{n}}}\frac{\partial^2\tilde{W}}{\partial\tilde{\mathbf{n}}\partial\hat{\mathbf{n}}},\end{aligned} \tag{15}$$

$$\tilde{U}_2 = \frac{2d'_{\tilde{\mathbf{n}}}}{\psi}\frac{\partial\tilde{U}}{\partial\tilde{\mathbf{n}}} + \frac{d_{\tilde{\mathbf{n}}}}{\psi}\frac{\partial^2\tilde{U}}{\partial\tilde{\mathbf{n}}^2} - \frac{d_{\tilde{\mathbf{n}}}d'_{\tilde{\mathbf{n}}}}{\psi^2}\frac{\partial\tilde{U}}{\partial\tilde{\mathbf{n}}}. \tag{16}$$

Multiplying both sides of equation (16) by $\psi$, we have

$$\psi\tilde{U}_2 = 2d'_{\tilde{\mathbf{n}}}\frac{\partial\tilde{U}}{\partial\tilde{\mathbf{n}}} + d_{\tilde{\mathbf{n}}}\frac{\partial^2\tilde{U}}{\partial\tilde{\mathbf{n}}^2} - d_{\tilde{\mathbf{n}}}\tilde{U}_3, \tag{17}$$

$$\tilde{U}_3 = \frac{d'_{\tilde{\mathbf{n}}}}{\psi}\frac{\partial\tilde{U}}{\partial\tilde{\mathbf{n}}}. \tag{18}$$

Then, multiplying both sides of equation (18) by $\psi$ yields

$$\psi\tilde{U}_3 = d'_{\tilde{\mathbf{n}}}\frac{\partial\tilde{U}}{\partial\tilde{\mathbf{n}}}. \tag{19}$$

Substituting $\psi = \mathrm{i}\omega + d_{\tilde{\mathbf{n}}}$ into equations (14), (15), (17), and (19), we obtain the following frequency domain equations:

$$\begin{aligned}&(\mathrm{i}\omega+d_{\tilde{\mathbf{n}}})\tilde{U}_3 = d'_{\tilde{\mathbf{n}}}\frac{\partial\tilde{U}}{\partial\tilde{\mathbf{n}}}, \\ &(\mathrm{i}\omega+d_{\tilde{\mathbf{n}}})\tilde{U}_2 = 2d'_{\tilde{\mathbf{n}}}\frac{\partial\tilde{U}}{\partial\tilde{\mathbf{n}}} + d_{\tilde{\mathbf{n}}}\frac{\partial^2\tilde{U}}{\partial\tilde{\mathbf{n}}^2} - d_{\tilde{\mathbf{n}}}\tilde{U}_3, \\ &(\mathrm{i}\omega+d_{\tilde{\mathbf{n}}})\tilde{U}_1 = (\lambda+2\mu)\left(d'_{\tilde{\mathbf{n}}}\frac{\partial\tilde{U}}{\partial\tilde{\mathbf{n}}} + 2d_{\tilde{\mathbf{n}}}\frac{\partial^2\tilde{U}}{\partial\tilde{\mathbf{n}}^2} - d_{\tilde{\mathbf{n}}}\tilde{U}_2\right) + (\lambda+\mu)d_{\tilde{\mathbf{n}}}\frac{\partial^2\tilde{W}}{\partial\tilde{\mathbf{n}}\partial\hat{\mathbf{n}}}, \\ &-\rho\omega^2\tilde{U} = (\lambda+2\mu)\frac{\partial^2\tilde{U}}{\partial\tilde{\mathbf{n}}^2} + \mu\frac{\partial^2\tilde{U}}{\partial\hat{\mathbf{n}}^2} + (\lambda+\mu)\frac{\partial^2\tilde{W}}{\partial\tilde{\mathbf{n}}\partial\hat{\mathbf{n}}} - \tilde{U}_1.\end{aligned} \tag{20}$$

Finally, transforming the above equations into the time-domain obtains

$$\begin{aligned}&(\partial_t+d_{\tilde{\mathbf{n}}})\tilde{u}_3 = d'_{\tilde{\mathbf{n}}}\frac{\partial\tilde{u}}{\partial\tilde{\mathbf{n}}}, \\ &(\partial_t+d_{\tilde{\mathbf{n}}})\tilde{u}_2 = 2d'_{\tilde{\mathbf{n}}}\frac{\partial\tilde{u}}{\partial\tilde{\mathbf{n}}} + d_{\tilde{\mathbf{n}}}\frac{\partial^2\tilde{u}}{\partial\tilde{\mathbf{n}}^2} - d_{\tilde{\mathbf{n}}}\tilde{u}_3, \\ &(\partial_t+d_{\tilde{\mathbf{n}}})\tilde{u}_1 = (\lambda+2\mu)\left(d'_{\tilde{\mathbf{n}}}\frac{\partial\tilde{u}}{\partial\tilde{\mathbf{n}}} + 2d_{\tilde{\mathbf{n}}}\frac{\partial^2\tilde{u}}{\partial\tilde{\mathbf{n}}^2} - d_{\tilde{\mathbf{n}}}\tilde{u}_2\right) + (\lambda+\mu)d_{\tilde{\mathbf{n}}}\frac{\partial^2\tilde{w}}{\partial\tilde{\mathbf{n}}\partial\hat{\mathbf{n}}}, \\ &\rho\partial_t^2\tilde{u} = (\lambda+2\mu)\frac{\partial^2\tilde{u}}{\partial\tilde{\mathbf{n}}^2} + \mu\frac{\partial^2\tilde{u}}{\partial\hat{\mathbf{n}}^2} + (\lambda+\mu)\frac{\partial^2\tilde{w}}{\partial\tilde{\mathbf{n}}\partial\hat{\mathbf{n}}} - \tilde{u}_1,\end{aligned} \tag{21}$$

where $\partial_t$ represents the time derivative. Equation (21) shows that the unsplit PML based on ADEs does

not need to split the fields, nor is it required to solve convolution or high-order temporal derivatives, which is more convenient for the ease of programming.

**The CFS-PML boundary condition for the slanted boundary**

The traditional stretching function has certain drawbacks, for example, at near-grazing incidence, seismic waves convert into evanescent waves, which travel parallel to the PML interface and cannot be effectively absorbed, thereby causing spurious reflections. In addition, the traditional stretching function attains singularity for very low-frequency waves. To enhance the absorption of the PML, the CFS stretching function has been proposed (Zhang and Shen, 2010):

$$s_{\tilde{\mathbf{n}}} = \chi_{\tilde{\mathbf{n}}} + \frac{d_{\tilde{\mathbf{n}}}}{\alpha_{\tilde{\mathbf{n}}} + \mathrm{i}\omega}. \tag{22}$$

Compared with equation (9), equation (22) has a more general form, including an attenuation factor $d_{\tilde{\mathbf{n}}}$, a frequency-shifted factor $\alpha_{\tilde{\mathbf{n}}}$ and a scaling factor $\chi_{\tilde{\mathbf{n}}}$. The frequency-shifted factor $\alpha_{\tilde{\mathbf{n}}}$ can shift the singularity in the stretching function from the real axis into the negative imaginary half of the complex plane, affecting the absorption of evanescent and low-frequency waves. The scaling factor $\chi_{\tilde{\mathbf{n}}}$ is more efficient in absorbing near-grazing incident waves (Zhang and Shen, 2010). $\alpha_{\tilde{\mathbf{n}}}$ and $\chi_{\tilde{\mathbf{n}}}$ are defined as

$$\begin{aligned} \alpha_{\tilde{\mathbf{n}}} &= \alpha_0 \left[ 1 - \left( \frac{l}{T} \right)^{p_\alpha} \right], \\ \chi_{\tilde{\mathbf{n}}} &= 1 + (\chi_0 - 1) \left( \frac{l}{T} \right)^{p_\chi}, \end{aligned} \tag{23}$$

where $P_\alpha = 1$ , $p_\chi = 2$, $\alpha_0 = \pi f_0$, and $f_0$ is the dominant frequency. Generally, $\chi_0 = 1$ guarantees the absorbing performance of the CFS-PML boundary condition such that the CFS stretching function becomes $s_{\tilde{\mathbf{n}}} = 1 + d_{\tilde{\mathbf{n}}} / \left( \alpha_{\tilde{\mathbf{n}}} + \mathrm{i}\omega \right)$.

As above, equation (8a) can be rewritten as

$$\begin{aligned} -\rho\omega^2 \tilde{U} = (\lambda + 2\mu) & \left\{ \begin{array}{l} -\dfrac{\left[ d'_{\tilde{\mathbf{n}}} (\alpha_{\tilde{\mathbf{n}}} + \mathrm{i}\omega) - d_{\tilde{\mathbf{n}}} \alpha'_{\tilde{\mathbf{n}}} \right] (\alpha_{\tilde{\mathbf{n}}} + \mathrm{i}\omega)}{(\alpha_{\tilde{\mathbf{n}}} + \mathrm{i}\omega + d_{\tilde{\mathbf{n}}})^3} \dfrac{\partial \tilde{U}}{\partial \tilde{\mathbf{n}}} \\ + \dfrac{(\alpha_{\tilde{\mathbf{n}}} + \mathrm{i}\omega)^2}{(\alpha_{\tilde{\mathbf{n}}} + \mathrm{i}\omega + d_{\tilde{\mathbf{n}}})^2} \dfrac{\partial^2 \tilde{U}}{\partial \tilde{\mathbf{n}}^2} \end{array} \right\} \\ & + \mu \frac{\partial^2 \tilde{U}}{\partial \hat{\mathbf{n}}^2} + (\lambda + \mu) \frac{\alpha_{\tilde{\mathbf{n}}} + \mathrm{i}\omega}{\alpha_{\tilde{\mathbf{n}}} + \mathrm{i}\omega + d_{\tilde{\mathbf{n}}}} \frac{\partial^2 \tilde{W}}{\partial \tilde{\mathbf{n}} \partial \hat{\mathbf{n}}}, \end{aligned} \tag{24}$$

where $\alpha'_{\tilde{\mathbf{n}}}$ is the first-order derivative of $\alpha_{\tilde{\mathbf{n}}}$ along the direction $\tilde{\mathbf{n}}$. Substituting $\psi = \alpha_{\tilde{\mathbf{n}}} + \mathrm{i}\omega + d_{\tilde{\mathbf{n}}}$ into equation (24), we obtain

$$\begin{aligned} -\rho\omega^2 \tilde{U} = & (\lambda + 2\mu) \frac{\partial^2 \tilde{U}}{\partial \tilde{\mathbf{n}}^2} + \mu \frac{\partial^2 \tilde{U}}{\partial \hat{\mathbf{n}}^2} + (\lambda + \mu) \frac{\partial^2 \tilde{W}}{\partial \tilde{\mathbf{n}} \partial \hat{\mathbf{n}}} \\ & - \left[ (\lambda + 2\mu) \left( \frac{d'_{\tilde{\mathbf{n}}}}{\psi} \frac{\partial \tilde{U}}{\partial \tilde{\mathbf{n}}} + \frac{2 d_{\tilde{\mathbf{n}}}}{\psi} \frac{\partial^2 \tilde{U}}{\partial \tilde{\mathbf{n}}^2} \right) + (\lambda + \mu) \frac{d_{\tilde{\mathbf{n}}}}{\psi} \frac{\partial^2 \tilde{W}}{\partial \tilde{\mathbf{n}} \partial \hat{\mathbf{n}}} \right] \\ & + (\lambda + 2\mu) d_{\tilde{\mathbf{n}}} \left( \frac{2 d'_{\tilde{\mathbf{n}}} + \alpha'_{\tilde{\mathbf{n}}}}{\psi^2} \frac{\partial \tilde{U}}{\partial \tilde{\mathbf{n}}} + \frac{d_{\tilde{\mathbf{n}}}}{\psi^2} \frac{\partial^2 \tilde{U}}{\partial \tilde{\mathbf{n}}^2} \right) \\ & - (\lambda + 2\mu) d_{\tilde{\mathbf{n}}}^2 \frac{d'_{\tilde{\mathbf{n}}} + \alpha'_{\tilde{\mathbf{n}}}}{\psi^3} \frac{\partial \tilde{U}}{\partial \tilde{\mathbf{n}}}. \end{aligned} \tag{25}$$

Introducing auxiliary variables,

$$\left\{ \begin{array}{l} \tilde{U}_3 = \dfrac{d'_{\tilde{\mathbf{n}}} + \alpha'_{\tilde{\mathbf{n}}}}{\psi} \dfrac{\partial \tilde{U}}{\partial \tilde{\mathbf{n}}}, \\ \tilde{U}_2 = \dfrac{2 d'_{\tilde{\mathbf{n}}} + \alpha'_{\tilde{\mathbf{n}}}}{\psi} \dfrac{\partial \tilde{U}}{\partial \tilde{\mathbf{n}}} + \dfrac{d_{\tilde{\mathbf{n}}}}{\psi} \dfrac{\partial^2 \tilde{U}}{\partial \tilde{\mathbf{n}}^2} - \dfrac{d_{\tilde{\mathbf{n}}}}{\psi} \tilde{U}_3, \\ \tilde{U}_1 = (\lambda + 2\mu) \left( \dfrac{d'_{\tilde{\mathbf{n}}}}{\psi} \dfrac{\partial \tilde{U}}{\partial \tilde{\mathbf{n}}} + \dfrac{2 d_{\tilde{\mathbf{n}}}}{\psi} \dfrac{\partial^2 \tilde{U}}{\partial \tilde{\mathbf{n}}^2} \right) \\ \quad + (\lambda + \mu) \dfrac{d_{\tilde{\mathbf{n}}}}{\psi} \dfrac{\partial^2 \tilde{W}}{\partial \tilde{\mathbf{n}} \partial \hat{\mathbf{n}}} - (\lambda + 2\mu) \dfrac{d_{\tilde{\mathbf{n}}}}{\psi} \tilde{U}_2. \end{array} \right. \tag{26}$$

Substituting $\psi = \alpha_{\tilde{\mathbf{n}}} + \mathrm{i}\omega + d_{\tilde{\mathbf{n}}}$ into equations (25) and (26), as well as transforming equations (25) and (26) back to the time-domain, yields

$$\begin{aligned} & (\alpha_{\tilde{\mathbf{n}}} + \partial_t + d_{\tilde{\mathbf{n}}}) \tilde{u}_3 = (d'_{\tilde{\mathbf{n}}} + \alpha'_{\tilde{\mathbf{n}}}) \frac{\partial \tilde{u}}{\partial \tilde{\mathbf{n}}}, \\ & (\alpha_{\tilde{\mathbf{n}}} + \partial_t + d_{\tilde{\mathbf{n}}}) \tilde{u}_2 = (2 d'_{\tilde{\mathbf{n}}} + \alpha'_{\tilde{\mathbf{n}}}) \frac{\partial \tilde{u}}{\partial \tilde{\mathbf{n}}} + d_{\tilde{\mathbf{n}}} \frac{\partial^2 \tilde{u}}{\partial \tilde{\mathbf{n}}^2} - d_{\tilde{\mathbf{n}}} \tilde{u}_3, \\ & (\alpha_{\tilde{\mathbf{n}}} + \partial_t + d_{\tilde{\mathbf{n}}}) \tilde{u}_1 = (\lambda + 2\mu) \left( d'_{\tilde{\mathbf{n}}} \frac{\partial \tilde{u}}{\partial \tilde{\mathbf{n}}} + 2 d_{\tilde{\mathbf{n}}} \frac{\partial^2 \tilde{u}}{\partial \tilde{\mathbf{n}}^2} \right) \\ & + (\lambda + \mu) d_{\tilde{\mathbf{n}}} \frac{\partial^2 \tilde{w}}{\partial \tilde{\mathbf{n}} \partial \hat{\mathbf{n}}} - (\lambda + 2\mu) d_{\tilde{\mathbf{n}}} \tilde{u}_2, \\ & \rho \partial_t^2 \tilde{u} = (\lambda + 2\mu) \frac{\partial^2 \tilde{u}}{\partial \tilde{\mathbf{n}}^2} + \mu \frac{\partial^2 \tilde{u}}{\partial \hat{\mathbf{n}}^2} + (\lambda + \mu) \frac{\partial^2 \tilde{w}}{\partial \tilde{\mathbf{n}} \partial \hat{\mathbf{n}}} - \tilde{u}_1. \end{aligned} \tag{27}$$

The entire process is divided into three parts. At each time step, the wavefield values at all stencil nodes are transformed using equation (7) and then $\tilde{u}_3$, $\tilde{u}_2$, and $\tilde{u}_1$ are updated in turn to obtain $\tilde{u}$ at the center node of the FD stencil. Finally, we inversely transform the wavefield values at all stencil nodes using

$$\begin{aligned} u &= \tilde{u}\cos\theta - \tilde{w}\sin\theta, \\ w &= \tilde{u}\sin\theta + \tilde{w}\cos\theta. \end{aligned} \tag{28}$$

## The corner node

For an absorbing-zone node $G$ expanded from the corner node, we assume an outward normal direction to be denoted by $\tilde{\mathbf{n}}$, as shown in Figure 2. Seismic waves

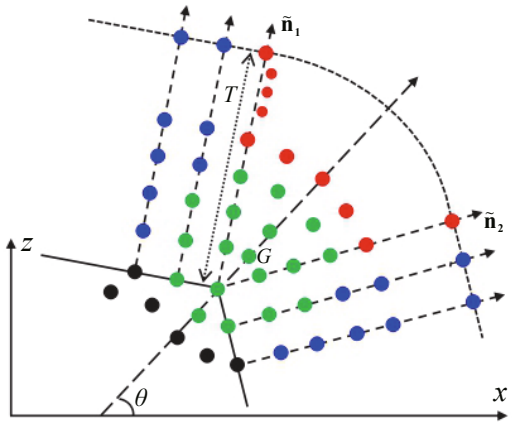


**Fig. 2 Illustration of expanding absorbing-zone nodes from the corner node.** The black dots represent mesh-free discrete nodes in the objective zone, blue dots are absorbing-zone nodes expanded based on the slanted boundaries, red dots are absorbing-zone nodes expanded based on the corner node, and green dots are all nodes in the FD stencil centered on node $G$.

are directly absorbed along the $x$ and $z$ axes.

**The PML boundary condition for the corner node**

For an absorbing-zone node $G$ expanded based on the corner node, we assume that the angle between the outward normal direction $\tilde{\mathbf{n}}$ and the positive $x$ axis is $\theta$. The elastic wave equation is transformed into a stretched-coordinate domain. The 2-D stretching function is written as (Drossaert and Giannopoulos, 2007)

$$s_\eta = 1 + \frac{d_\eta}{\mathrm{i}\omega}, \tag{29}$$

where $\eta = x, z$. The attenuation factors are

$$\begin{cases} d_x = d_{\tilde{\mathbf{n}}} \sin\left(\pi/2 - \theta\right)^2, \\ d_z = d_{\tilde{\mathbf{n}}} \sin\left(\theta\right)^2. \end{cases} \tag{30}$$

By constructing ADEs, we obtain the time-domain PML formulations for the corner node:

$$\begin{aligned}
&(\partial_t + d_x)u_{x3} = d_x' \frac{\partial u}{\partial x}, \\
&(\partial_t + d_x)u_{x2} = d_x \frac{\partial^2 u}{\partial x^2} + 2d_x' \frac{\partial u}{\partial x} - d_x u_{x3}, \\
&(\partial_t + d_x)u_{x1} = (\lambda+\mu) d_x \frac{\partial^2 w}{\partial x \partial z} \\
&\qquad + (\lambda + 2\mu)\left( d_x' \frac{\partial u}{\partial x} + 2d_x \frac{\partial^2 u}{\partial x^2} - d_x u_{x2} \right), \\
&(\partial_t + d_z)u_{z3} = d_z' \frac{\partial u}{\partial z}, \\
&(\partial_t + d_z)u_{z2} = d_z \frac{\partial^2 u}{\partial z^2} + 2d_z' \frac{\partial u}{\partial z} - d_z u_{z3}, \\
&(\partial_t + d_z)u_{z1} = (\lambda+\mu) d_z \frac{\partial^2 w}{\partial x \partial z} \\
&\qquad + \mu\left( d_z' \frac{\partial u}{\partial z} + 2d_z \frac{\partial^2 u}{\partial z^2} - d_z u_{z2} \right), \\
&(\partial_t + d_z)u_{xz2} = d_z \frac{\partial^2 w}{\partial x \partial z}, \\
&(\partial_t + d_x)u_{xz1} = (\lambda+\mu) d_x u_{xz2}, \\
&\rho \partial_t^2 u = (\lambda + 2\mu)\frac{\partial^2 u}{\partial x^2} + \mu \frac{\partial^2 u}{\partial z^2} \\
&\qquad + (\lambda+\mu)\frac{\partial^2 w}{\partial x \partial z} - u_{x1} - u_{z1} + u_{xz1},
\end{aligned} \tag{31}$$

where $u_{x3}$, $u_{x2}$, $u_{x1}$, $u_{z3}$, $u_{z2}$, $u_{z1}$, $u_{xz2}$ and $u_{xz1}$ are auxiliary variables.

**The CFS-PML boundary condition for the corner node**

The CFS stretching function in a Cartesian coordinate system can be written as (Zhang and Shen, 2010)

$$s_\eta = \chi_\eta + \frac{d_\eta}{\alpha_\eta + \mathrm{i}\omega}, \tag{32}$$

where

$$\begin{aligned}
\alpha_x &= \alpha_0 \left[ 1 - \left( \frac{l}{T} \right)^{p_\alpha} \sin(\pi/2 - \theta)^{p_\alpha} \right], \\
\alpha_z &= \alpha_0 \left[ 1 - \left( \frac{l}{T} \right)^{p_\alpha} \sin(\theta)^{p_\alpha} \right], \\
\chi_x &= 1 + (\chi_0 - 1)\left( \frac{l}{T} \right)^{p_\chi} \sin(\pi/2 - \theta)^{p_\chi}, \\
\chi_z &= 1 + (\chi_0 - 1)\left( \frac{l}{T} \right)^{p_\chi} \sin(\theta)^{p_\chi}.
\end{aligned} \tag{33}$$

As above, $\chi_0 = 1$ such that the CFS stretching function becomes $s_\eta = 1 + d_\eta / (\alpha_\eta + \mathrm{i}\omega)$.

By constructing ADEs, we obtain time-domain CFS-PML formulations for the corner node as follows:

$$
\begin{aligned}
&(\alpha_x + \partial_t + d_x)u_{x3} = (d_x' + \alpha_x')\frac{\partial u}{\partial x},\\
&(\alpha_x + \partial_t + d_x)u_{x2} = d_x\frac{\partial^2 u}{\partial x^2} + (2d_x' + \alpha_x')\frac{\partial u}{\partial x} - d_x u_{x3},\\
&(\alpha_x + \partial_t + d_x)u_{x1} = (\lambda+\mu)d_x\frac{\partial^2 w}{\partial x \partial z}\\
&\qquad + (\lambda + 2\mu)\left(d_x'\frac{\partial u}{\partial x} + 2d_x\frac{\partial^2 u}{\partial x^2} - d_x u_{x2}\right),\\
&(\alpha_z + \partial_t + d_z)u_{z3} = (d_z' + \alpha_z')\frac{\partial u}{\partial z},\\
&(\alpha_z + \partial_t + d_z)u_{z2} = d_z\frac{\partial^2 u}{\partial z^2} + (2d_z' + \alpha_z')\frac{\partial u}{\partial z} - d_z u_{z3},\\
&(\alpha_z + \partial_t + d_z)u_{z1} = (\lambda+\mu)d_z\frac{\partial^2 w}{\partial x \partial z} + \mu\left(d_z'\frac{\partial u}{\partial z} + 2d_z\frac{\partial^2 u}{\partial z^2} - d_z u_{z2}\right),\\
&(\alpha_z + \partial_t + d_z)u_{xz2} = d_z\frac{\partial^2 w}{\partial x \partial z},\\
&(\alpha_x + \partial_t + d_x)u_{xz1} = (\lambda+\mu)d_x u_{xz2},\\
&\rho\partial_t^2 u = (\lambda+2\mu)\frac{\partial^2 u}{\partial x^2} + \mu\frac{\partial^2 u}{\partial z^2} + (\lambda+\mu)\frac{\partial^2 w}{\partial x \partial z} - u_{x1} - u_{z1} + u_{xz1}.
\end{aligned}
\tag{34}
$$

Equations (31) and (34) demonstrate that ADEs are first-order equations. During the time marching process, the values of auxiliary variables at the next time step directly cover values at the current time step, saving computer memory.

# Numerical examples

To demonstrate the effectiveness of both PML boundary conditions and the utility of the CFS-PML, we conducted RBF-FD numerical simulations for homogeneous, multi-layer, and truncated Hess models. The nodal distribution in the objective zone was obtained using the fast-generation algorithm (Fornberg and Flyer, 2015), whereas the nodal distribution of the absorbing-zone was obtained using the expanding strategy.

## The polygonal homogeneous model

As shown in Figure 3, the polygonal homogeneous model has a slanted boundary and five corner nodes; zone I is the objective zone, zones II are absorbing zones generated based on straight boundaries, zones III are absorbing zones generated from corner nodes. P-wave velocity is 5000 m/s, S-wave velocity is 3000 m/s, and density is 2800 kg/m$^3$. We adopted a quasi-uniform nodal distribution in the objective zone, and the "grain radius" was set at 10 m. We used RBF-FD to simulate elastic wave propagation and the number of neighboring nodes in each FD stencil was set at 20. The point source was a concentrated force source with an angle of 135° counterclockwise from the $z$ axis. The source wavelet was a 25 Hz Ricker wavelet. The time step used was 0.001 s. Two sources $S_1$ and $S_2$ are located at (1500, 500) m and (800, 10) m. Receivers $R_1$ and $R_2$ are located at (2000, 10) m and (800, 1000) m. We conducted RBF-FD numerical simulations on polygonal homogeneous models using source $S_1$ and 20 absorbing layers. Figure 4 shows snapshots of the vertical component at 0.2 and 0.42 s demonstrating clearly that both PML boundary conditions have excellent absorbing performances.

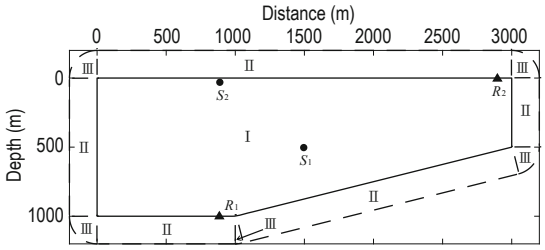


**Fig. 3 Diagram of the polygonal homogeneous model. Dots indicate the positions of sources and triangles indicate receivers.**

To demonstrate the advantageous utility of the CFS-PML using source $S_2$, we performed RBF-FD numerical simulations on polygonal homogeneous models. The number of the absorbing layers was 8. The source was close to the top boundary to allow the formation of near-grazing incident waves. The angle of the concentrated force source was selected to ensure that P-wave and S-wave impinge onto the PML interface at either the normal or near-grazing angle. Figure 5 shows snapshots of the vertical component at 0.3, 0.5, and 0.7 s. One can clearly observe that, as simulation time increases, large offset and large-angle incident waves appear. Seismic waves are converted into evanescent waves that travel parallel to the PML interface, causing spurious reflections. Furthermore, the stretching function becomes singular for low frequencies or waves with a long-term interaction with the PML interface, again resulting in spurious reflections. The CFS-PML boundary condition using the CFS stretching function exhibits better absorption for large-angle incident waves, such that there are almost no spurious reflections, even at very large offset values. To further verify these conclusions, we compare waveforms recorded at two receivers for

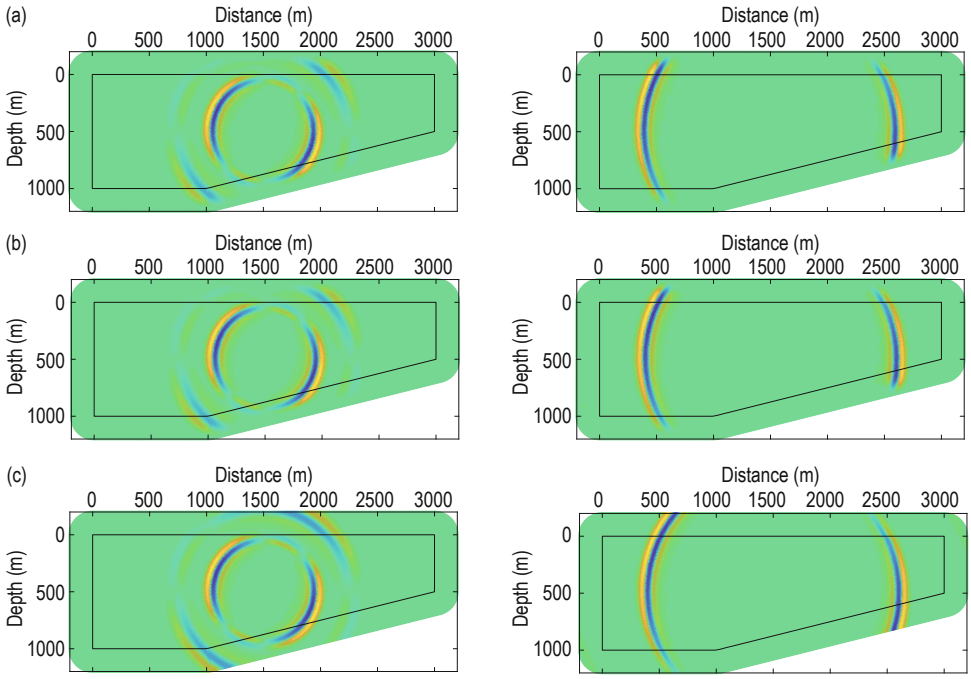


**Fig. 4 Snapshots of the vertical component using source $S_1$ at 0.2 s (left) and 0.42 s (right). (a) The proposed PML. (b) The proposed CFS-PML. (c) Reference snapshots computed by extending the model boundaries. The black lines represent internal boundaries of the absorbing-zone.**

both the cases of PML and CFS-PML. The waveforms at receiver $R_1$ in Figure 6 show that both PML boundary conditions exhibit good absorption for normal incident waves. The waveforms at receiver $R_2$ show that at large offsets, seismic waves impinge upon the PML interface at near-grazing angles, and the PML waveforms have

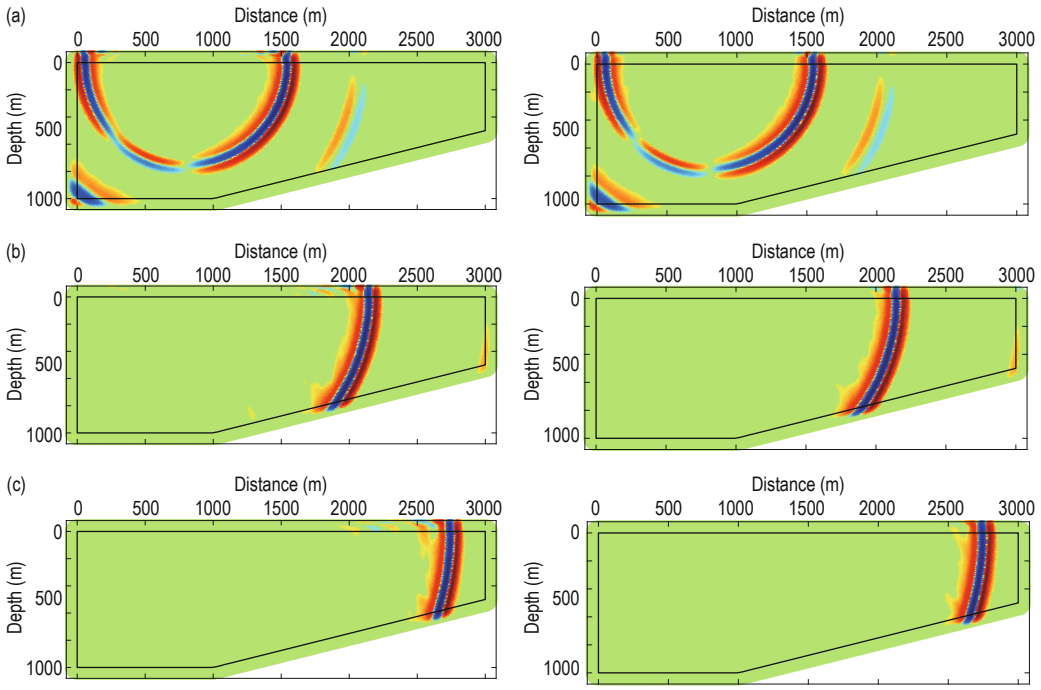


**Fig. 5 Snapshots of the vertical component using the source $S_2$ at 0.3 s (a), 0.5 s (b), and 0.7 s (c). Figures on the left are snapshots of the proposed PML, and figures on the right are snapshots of the proposed CFS-PML. The cutoff threshold is 2.5% of the maximum value in the corresponding snapshot, and the normalized value is raised to the power of 0.3 to enhance small amplitudes. The amplitude is displayed in red (positive) and blue (negative) at each node.**

obvious spurious oscillations, whereas the CFS-PML waveforms remain in good agreement with the reference waveforms. The reference waveforms are computed by extending the model boundaries. Therefore, the CFS-PML has better absorption for near-grazing incident and evanescent waves. These conclusions are similar to those of previous papers (Drossaert and Giannopoulos, 2007; Komatitsch and Martin, 2007; Zhang et al., 2009); however, although the CFS-PML boundary conditions use the CFS stretching function in the coordinate transformation, they are implemented in different ways.

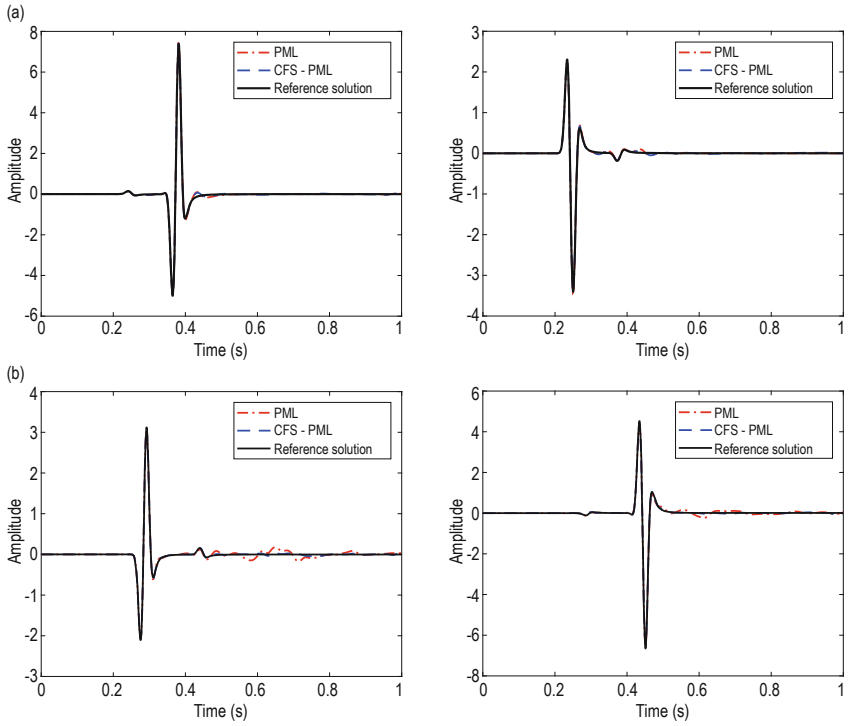


**Fig. 6 Waveforms at receivers using source $S_2$. (a) Receiver $R_1$. (b) Receiver $R_2$. Vertical and horizontal components are from left to right.**

## The non-rectangular multi-layer model

Figure 7a shows a rectangular multi-layer model where the P-wave velocities are 2500, 4000, and 5000 m/s and S-wave velocities are 1500, 2700, and 3500 m/s, from shallow to deep. The density is 2800 kg/m$^3$. Mesh-free FD simulations need to predetermine the FD coefficients for each stencil in advance, resulting in significant computational costs. For RBF-FD, the FD coefficients are fixed provided that the relative positions of nodes in the stencils remain the same. Therefore, we discretize the velocity model with regularly arranged nodes and then insert scattered nodes that perfectly fit model interfaces and boundaries. Finally, an efficient "node repel" algorithm is used to adjust the positions of neighboring nodes to show the location of given interfaces and boundaries (Fornberg and Flyer, 2015). Figure 7b shows nodal distributions in the multi-layer model, i.e., nodes are evenly distributed with an average node spacing of 5 m. Because RBF-FD can accurately simulate seismic wave propagation in the non-rectangular computational domain, we cut off the lower left and right regions of the rectangular multi-layer model. Figure 8 shows the non-rectangular multi-layer model and its mesh-free nodal distribution. The red zones show the absorbing-zone nodal distribution generated from corner nodes, blue zones show the absorbing-zone nodal distribution generated from straight boundaries, and black and cyan zones show nodal distributions in the objective zone. The FD stencils centered on each node in the cyan zone have the same FD coefficients because the relative positions of nodes in these stencils are the same. We are required to predetermine the FD coefficients of any one of these stencils.

We used an explosive source located at (1500, 50) m with a 30 Hz Ricker source wavelet and a time step of 0.0005 s. The receivers were placed with 5 m intervals at a depth of 50 m. The thickness of the absorbing-zone was 100 m, and the number of the absorbing layers was 20. On the basis of two proposed PML

boundary conditions, we performed RBF-FD numerical simulations on rectangular and non-rectangular multi-layer models. The total number of nodes in each FD stencil was 21. Coefficient matrices of RBF-FD included a first-order polynomial to improve their convergence rate. Furthermore, on the basis of the proposed unsplit CFS-PML, we also performed regular-grid numerical simulations on a rectangular multi-layer model, which has dimensions of 3000 m × 2000 m. We considered a 10th-order-accuracy FD in regular-grid simulations such that the number of grid points in each regular-grid FD stencil was the same as the number of nodes in the RBF-FD stencil. The regular-grid simulation has grid sizes of 5 m × 5 m and 2 m × 2 m and 20 absorbing layers.

Figure 9 illustrates the nodal distributions of dash-square regions in Figure 8a. Figure 10 displays seismograms computed by regular-grid FD. Since the grids in regular-grid simulations are regularly arranged, the staircase approximation for curved interfaces will inevitably lead to scattering noise, as shown in Figure 10a. To circumvent such problems, the grid size was generally reduced, but this leads to an increase in computational cost. Figure 10b shows the seismogram obtained using a smaller grid size (2 m × 2 m), but some visible scattering noises are still visible. The mesh-free nodal distribution can exactly depict the location of interfaces and boundaries, and avoid scattering noises, as shown in Figure 11. In addition, there are no visible spurious reflections, validating the effectiveness of the two PML methods. Long-term simulation can verify the numerical stability of the two PML boundary conditions. Table 1 shows the memory costs (in terms of the number of nodes) required by RBF-FD simulations for rectangular and non-rectangular multi-layer models.

**Table 1 Memory costs (in terms of the number of nodes) required by RBF-FD simulations for rectangular and non-rectangular multi-layer models**

| | Rectangular multi-layer model | | Non-rectangular multi-layer model | |
|---|---|---|---|---|
| Objective zone | 53176 (Black zone) | 187516 (Cyan zone) | 48314 (Black zone) | 164216 (Cyan zone) |
| Absorbing zone | 1400(Red zone) | 39920 (Blue zone) | 1440 (Red zone) | 36040 (Blue zone) |

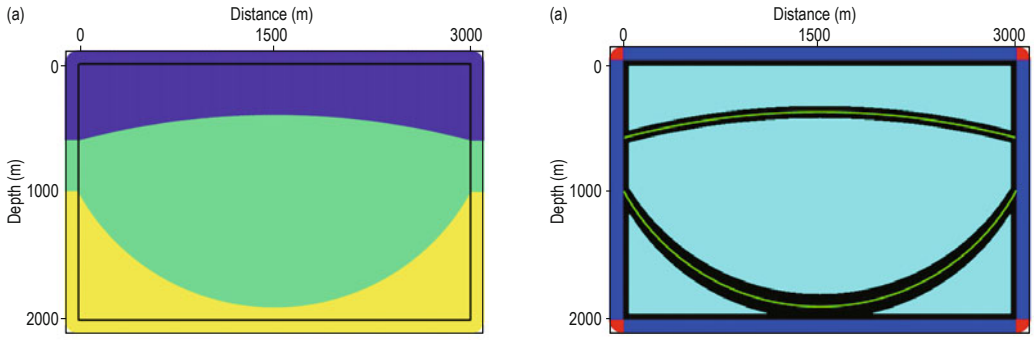


**Fig. 7 The rectangular multi-layer model (a) and its mesh-free nodal distribution (b). Black lines represent the internal boundaries of the absorbing-zone; solid green lines represent the internal curved interfaces of the model.**

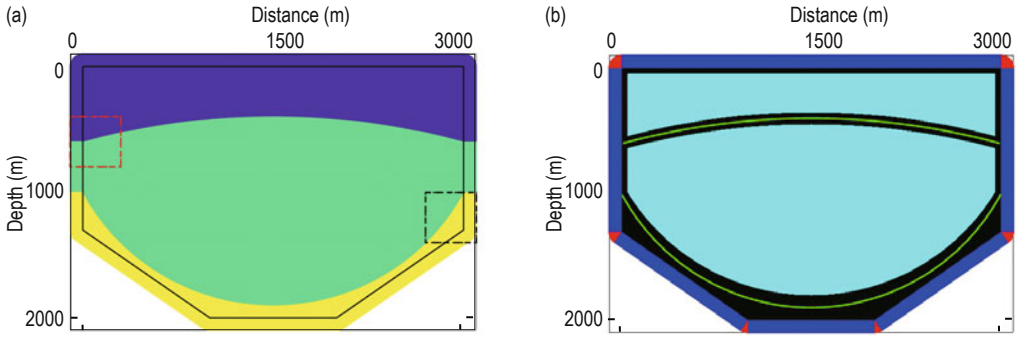


**Fig. 8 The non-rectangular multi-layer model (a) and its mesh-free nodal distribution (b). Black lines represent internal boundaries of the absorbing-zone; solid green lines represent the internal curved interfaces of the model.**

Figure 12 shows normalized computational times for RBF-FD numerical simulations running the same number of time steps. All simulations were performed on the same computer (Dell with Inter(R) Core(TM) i7-4770 3.4 GHz CPU and 8GB memory) using MATLAB. This reveals that by removing unnecessary areas of the model and incorporating the two proposed PML boundary conditions, the computational cost can be significantly reduced and the mesh-free FD modeling efficiency can be improved dramatically.

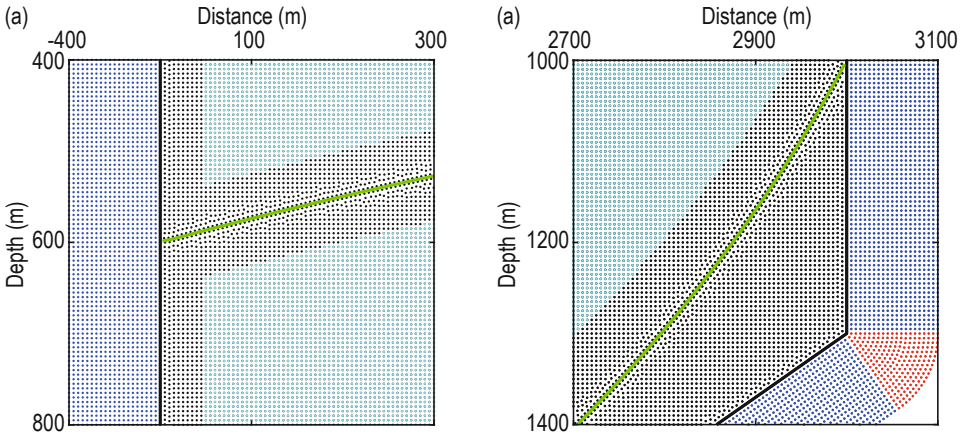


**Fig. 9 Nodal distributions of the dash-square regions. (a) The red dash-square region. (b) The black dash-square region.**

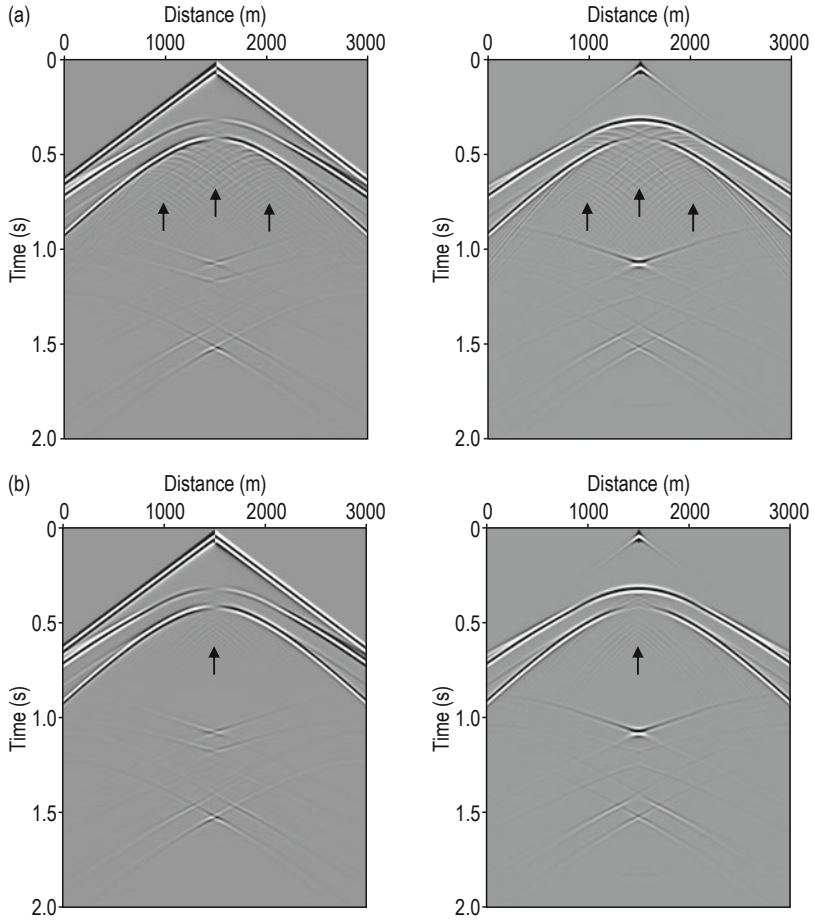


**Fig. 10 Seismograms computed using regular-grid FD for the rectangular multi-layer model. (a) 5 m × 5 m. (b) 2 m × 2 m. Figures on the left show seismograms of the horizontal component, and figures on the right show seismograms of the vertical component.**

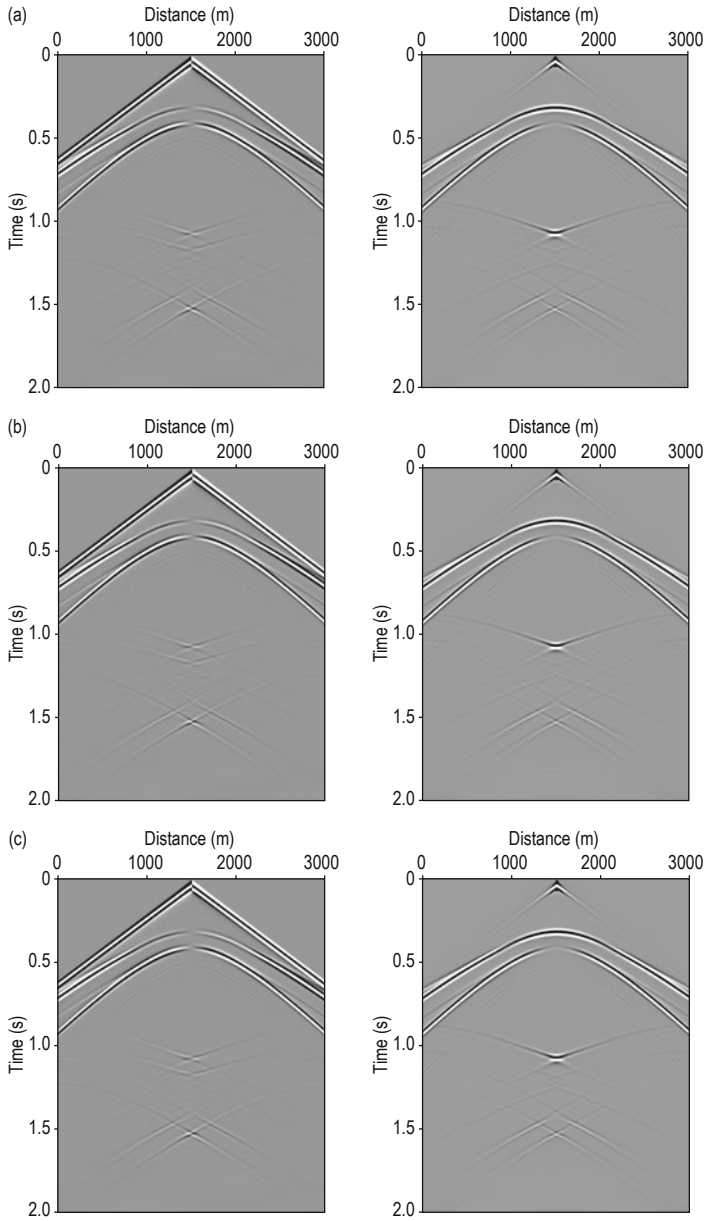


**Fig. 11 Seismograms computed using RBF-FD for the multi-layer velocity model. (a) Rectangular multi-layer model (CFS-PML). (b) Non-rectangular multi-layer model (CFS-PML). (c) Non-rectangular multi-layer model (PML). Figures on the left show seismograms of the horizontal component, and figures on the right show seismograms of the vertical component.**

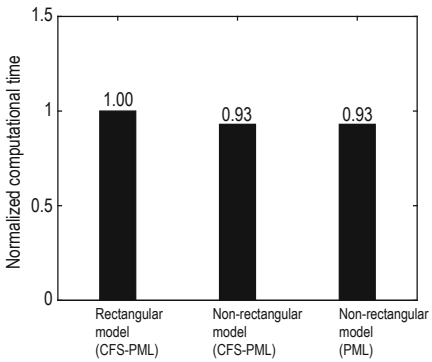


**Fig. 12 Normalized computational times for RBF-FD numerical simulations running the same number of time steps.**

## The truncated Hess model

The fast-generation algorithm is an advancing-front type algorithm. The "grain radius," a parameter controlling nodal density, can be obtained based on the model velocity and may be used to generate a model-adaptive nodal distribution of variable-density. In mesh-free FD simulations, nodal density increases as wave velocity decreases, achieving local refinement in critical areas and reducing computational costs.

Figure 13 shows a truncated Hess model with the lower left and right regions removed. Note that this

model is used only to demonstrate the effectiveness of two PML boundary conditions without rigorous geological consideration. In order to avoid sudden changes in nodal density that may lead to instability throughout long-time simulations, we smoothed the velocity model. Figure 14 displays the variable-density nodal distribution in the truncated Hess model. The "grain radius" ranges from 10 to 15 m with respect to the S-wave velocity range of 1600 to 3200 m/s. Velocities of 1600 and 3200 m/s correspond to "grain radii" of 10 and 15 m, respectively. The density was set at 2800 kg/m$^3$.

An explosive source with a 15 Hz Ricker source wavelet located at (2500, 50) m was used. The time step was 0.0005 s. Receivers were placed with 10 m intervals at a depth of 50 m. The thickness of the absorbing-zone was 300 m, and the minimum number of the absorbing layers was 20. We performed RBF-FD numerical simulations on the Hess model using two proposed PML boundary conditions. The number of nodes in each FD stencil was 21. We also performed regular-grid numerical simulations on a rectangular Hess model with dimension of 5000 m × 3000 m. We used a 10th-order-accuracy FD

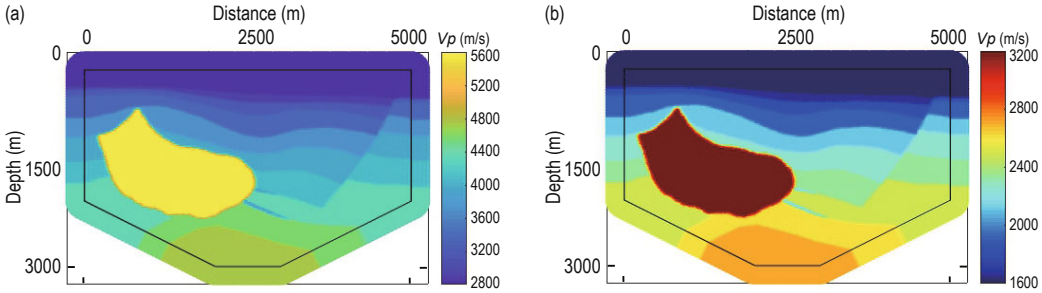


**Fig. 13 The truncated Hess model. (a) P-wave velocity. (b) S-wave velocity.**

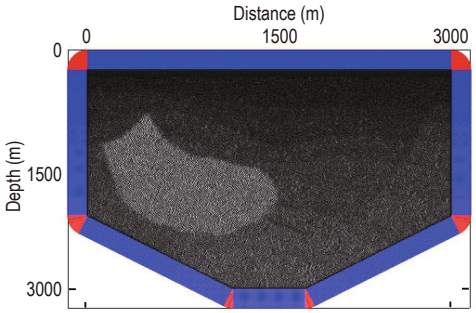


**Fig. 14 The variable-density nodal distribution in the truncated Hess model. The black zone shows the nodal distribution in the objective zone, blue zones show the absorbing-zone nodal distribution generated based on straight boundaries, and red zones show the absorbing-zone nodal distribution generated from the corner nodes.**

in regular-grid simulation such that the number of grid points in each regular-grid FD stencil was equivalent to the number of nodes in the RBF-FD stencil. The grid size was 10 m × 10 m, and the number of the absorbing layers was 20.

Figure 15 shows seismograms computed by RBF-FD and regular-grid FD. Almost no difference was observed between the results shown in Figures 15a, 15b, and 15c. Figure 16 displays trace number 401 from Figure 15. The waveforms of RBF-FD coincide with those of regular-grid FD. These numerical results validate the accuracy of RBF-FD for solving seismic wave equations and further validate two proposed PML boundary conditions for the slanted boundary with large variations in velocity.

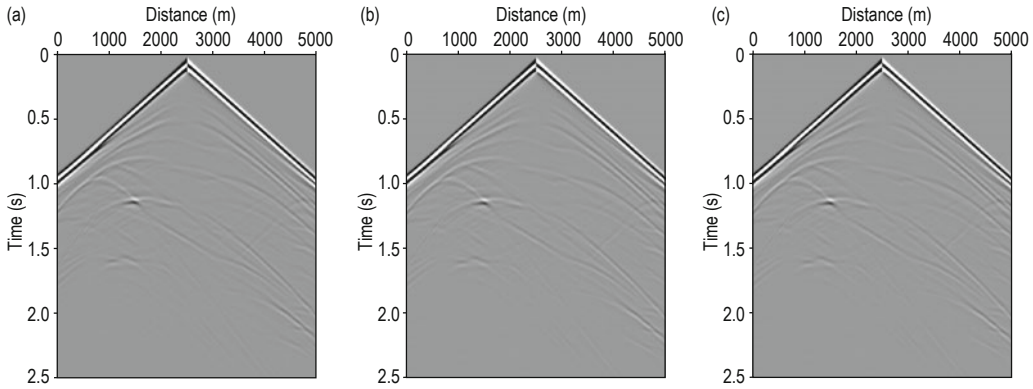


**Fig. 15 Seismograms of the horizontal component in the Hess velocity model. (a) Regular-grid FD (10 m × 10 m, CFS-PML). (b) RBF-FD (CFS-PML). (c) RBF-FD (PML).**

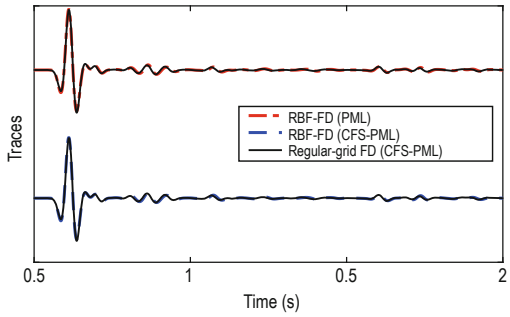


**Fig. 16 Sampled traces from seismograms (trace 401) shown in Figure 15.**

## Conclusions

In this paper, we developed PML and CFS-PML boundary conditions for mesh-free FD solution of the elastic wave equation. These conditions can effectively eliminate spurious reflections without convolution or wave field splitting. The proposed PML boundary conditions are applicable to vertical and horizontal boundaries, in addition to slanted boundaries. Through using RBF-FD and two proposed PML boundary conditions, we perform elastic wave numerical simulations on the polygonal homogeneous model, the non-rectangular multi-layer model, and then truncated Hess model. We make the following conclusions:

(1) These two PML boundary conditions can be applied to horizontal, vertical and slanted boundaries to obtain good absorption. For near-grazing incident waves and very low-frequency waves, the performance of the PML is severely reduced, but the proposed CFS-PML continues to maintain good absorption.

(2) The mesh-free nodal distribution can exactly depict the location of interfaces and boundaries and thus improve modeling accuracy. As one of the most popular mesh-free FD methods, RBF-FD can successfully simulate wave propagation in the non-rectangular computational domain. By removing unnecessary areas of the model and incorporating variable-density nodal distribution together with the two proposed PML boundary conditions, we have improved the mesh-free FD modeling efficiency while ensuring accuracy.

The objective zone may have a smooth curved boundary. If the absorbing-zone nodal distribution is directly generated from a smooth curved boundary using the straightforward expanding strategy, the distance between two adjacent nodes of the outermost absorbing layer will not be equal to the initial distance between two adjacent boundary nodes. In this case, both the PML and CFS-PML boundary conditions can absorb incident elastic waves but cannot guarantee stability throughout long-time simulations. For a convex boundary, some regions outside the boundary require filling to form boundaries consisting of two or more straight boundaries. For a concave boundary, the caved-in region must be filled to form a straight boundary. Regardless of whether the boundary is convex or concave, it is necessary to fill some regions outside the curved boundary to form a polygonal objective zone with straight boundaries.

## References

Alford, R. M., Kelly, K. R., and Boore, D. M., 1974, Accuracy of finite-difference modeling of the acoustic wave equation: Geophysics, **39**(6), 834–842.

Bayona, V., Flyer, N., Fornberg, B., et al., 2017, On the role of polynomials in RBF-FD approximations—Part 2: Numerical solution of elliptic PDEs: Journal of Computational Physics, **332**, 257–273.

Bérenger, J. P., 1994, A perfectly matched layer for the absorption of electromagnetic waves: Journal of Computational Physics, **114**(2), 185–200.

Chew, W. C., and Liu, Q. H., 1996, Perfectly matched layers for elastodynamics: A new absorbing boundary condition: Journal of Computational Acoustics, **4**(4), 341–359.

Chew, W. C., and Weedon, W. H., 1994, A 3D perfectly matched medium from modified Maxwell's equations with stretched coordinates: Microwave and Optical Technology Letters, **7**(13), 599–604.

Driscoll, T. A., and Fornberg, B., 2002, Interpolation in the limit of increasingly flat radial basis functions: Computers & Mathematics with Applications, **43**(3), 413–422.

Drossaert, F. H., Giannopoulos, A., 2007, A nonsplit complex frequency-shifted PML based on recursive integration for FDTD modeling of elastic waves: Geophysics, **72**(2), T9–T17.

Flyer, N., Barnett, G. A., and Wicker, L. J., 2016a, Enhancing finite differences with radial basis functions: Experiments on the Navier-Stokes equations: Journal of Computational Physics, **316**, 39–62.

Flyer, N., Fornberg, B., Bayona, V., et al., 2016b, On the role of polynomials in RBF-FD approximations—Part 1: Interpolation and accuracy: Journal of Computational Physics, **321**, 21–38.

Flyer, N., Lehto, E., Blaise, S., et al., 2012, A guide

to RBF-generated finite differences for nonlinear transport: shallow water simulations on a sphere: Journal of Computational Physics, **231**, 4078–4095.

Flyer, N., Wright, G. B., and Fornberg, B., 2014, Radial basis function-generated finite differences: a mesh-free method for computational geosciences, in Freeden, W., Nashed, M. Z., and Sonar, T., Eds., Handbook of Geomathematics: Springer, 1–30.

Fornberg, B., Flyer, N., 2015, Fast generation of 2-D node distributions for mesh-free PDE discretizations: Computers & Mathematics with Applications, **69**(7), 531–544.

Fornberg, B., Lehto, E., and Powell, C., 2013, Stable calculation of Gaussian-based RBF-FD stencils: Computers & Mathematics with Applications, **65**, 627–637.

Gao, Y., Zhang, J., and Yao, Z., 2015, Unsplit complex frequency shifted perfectly matched layer for second-order wave equation using auxiliary differential equations: The Journal of the Acoustical Society of America, **138**(6), EL551–EL557.

Hestholm, S., 1999, Three-dimensional finite difference viscoelastic wave modelling including surface topography: Geophysical Journal International, **139**(3), 852–878.

Komatitsch, D., and Martin, R., 2007, An unsplit convolutional perfectly matched layer improved at grazing incidence for the seismic wave equation: Geophysics, **72**(5), SM155–SM167.

Komatitsch, D., and Tromp, J., 2003, A perfectly matched layer absorbing boundary condition for the second-order seismic wave equation: Geophysical Journal International, **154**(1), 146–153.

Kosloff, D., and Baysal, E., 1982, Forward modeling by a Fourier method: Geophysics, **47**(10), 1402–1412.

Kristek, J., Moczo, P., Galis, M., 2010, Stable discontinuous staggered grid in the finite-difference modeling of seismic motion: Geophysical Journal International, **183**(3), 1401–1407.

Kuzuoglu, M., and Mittra, R., 1996, Frequency dependence of the constitutive parameters of causal perfectly matched anisotropic absorbers: IEEE Microwave and Guided Wave Letters, **6**(12), 447–449.

Larsson, E., Lehto, E., Heryodono, A., et al., 2013, Stable calculation of differentiation matrices and scattered node stencils based on Gaussian radial basis functions: SIAM Journal on Scientific Computing, **35**, A2096–A2119.

Lee, Y. J., Micchelli, G. J., and Yoon, J., 2014, On convergence of flat multivariate interpolation by translation kernels with finite smoothness: Constructive Approximation, **40**(1), 37–60.

Li, B., Liu, Y., Sen, M. K., et al., 2017a, Time-space-domain mesh-free finite difference based on least squares for 2D acoustic-wave modeling: Geophysics, **82**(4), T143–T157.

Li, B., Liu, Y., Zhao, Y., et al., 2017b, Hybrid absorbing boundary condition for piecewise smooth curved boundary in 2D acoustic finite difference modelling: Exploration Geophysics, **49**(4), 469–483.

Ma, Y., Yu, J., Wang, Y., 2014, A novel unsplit perfectly matched layer for the second-order acoustic wave equation: Ultrasonics, **54**(6), 1568–1574.

Martin, B., Flyer, N., Fornberg, B., et al., 2013, Development of mesh-less computational algorithms for seismic exploration: 83th SEG Technical Program Expanded Abstracts, 3543–3547.

Martin, B., Fornberg, B., and St-Cyr, A., 2015, Seismic modeling with radialbasis-function-generated finite differences: Geophysics, **80**(4), T137-T146.

O'Brien, G. S., and Bean, C. J., 2011, An irregular lattice method for elastic wave propagation: Geophysical Journal International, **187**(3), 1699–1707.

Seron, F. J., Sanz, F. J., Kindelan, M., et al., 1990, Finite-element method for elastic wave propagation: Communications in Applied Numerical Methods, **6**(5), 359–368.

Shankar, V., Wright, G. B., Kirby, R. M., et al., 2015, A radial basis function (RBF)-finite difference (FD) method for diffusion and reaction-diffusion equations on surfaces: Journal Scientific Computing, **63**(3), 745–768.

Roden, J. A., and Gedney, S. D., 2000, Convolution PML (CPML): an efficient FDTD implementation of the CFS-PML for arbitrary media: Microwave and Optical Technology Letters, **27**(5), 334–339.

Takekawa, J., and Mikada, H., 2016, An absorbing boundary condition for acoustic-wave propagation using a mesh-free method: Geophysics, **81**(4), T145–T154.

Takekawa, J., and Mikada, H., 2018, A mesh-free finite-difference method for elastic wave propagation in the frequency-domain: Computers and Geosciences, **118**, 65–78.

Virieux, J., 1986, P-SV wave propagation in heterogeneous media: velocity-stress finite-difference method: Geophysics, **51**(4), 889–901.

Wang, T., and Tang, X. M., 2003, Finite-difference modeling of elastic wave propagation: A nonsplitting perfectly matched layer approach: Geophysics, **68**(5), 1749–1755.

Zhang, J., and Liu, T., 2002, Elastic wave modelling

in 3D heterogeneous media: 3D grid method: Geophysical Journal International, 150(3), 780–799.

Zhang, L. X., Fu, L. Y., and Pei, Z. L., 2010, Finite difference modeling of Biot's poroelastic equations with unsplit convolutional PML and rotated staggered grid: Chinese Journal of Geophysics (in Chinese), **53**(10), 2470–2483.

Zhang, W., Chen, X., 2006, Traction image method for irregular free surface boundaries in finite difference seismic wave simulation: Geophysical Journal International, **167**(1), 337–353.

Zhang, W., and Shen, Y., 2010, Unsplit complex frequency-shifted PML implementation using auxiliary differential equations for seismic wave modeling: Geophysics, **75**(4), T141–T154.

Zhang, X. W., Han, L. G., Huang, L., et al., 2009, A staggered-grid high-order difference method of complex frequency-shifted PML based on recursive integration for elastic wave equation: Chinese Journal of Geophysics (in Chinese), **52**(7), 1800–1807.

Corresponding author: **Sun Cheng-Yu**, graduated from

University of Petroleum at 1992 and obtain his doctoral degree at 2001. Now he is a professor of China University of Petroleum (East China) and works on teaching and research of seismic wave theory and prospecting technology (Email: suncy@upc.edu.cn).